RSC Advances

PAPER

View Article Online
View Journal | View Issue

Cite this: *RSC Adv.*, 2026, **16**, 25229

High-clarity multifunctional Cu/Ni transparent films for efficient electromagnetic interference shielding

Xiaolin Li,[a] Dianyu Wu,[b] Xiaoli Xu[b] and Wenping Geng *[a]

Transparent conductive materials still face significant challenges in simultaneously achieving high optical transmittance, broadband electromagnetic interference (EMI) shielding, and excellent environmental stability. In this work, a hexagonal–Voronoi composite metal mesh (HV-CMM) is proposed by integrating a periodic hexagonal framework with stochastic Voronoi substructures, which effectively suppresses optical diffraction while maintaining structural stability. By tuning the characteristic size of the Voronoi features, a synergistic optimization of optical and electromagnetic performance is achieved. The fabricated HV-CMM exhibits high optical transmittance of 78–83% and low haze of 4.5–4.8% in the visible range. Owing to the disruption of long-range periodicity, coherent diffraction is effectively suppressed, leading to improved visual uniformity. In the 1–18 GHz frequency range, the samples demonstrate stable EMI shielding performance, with an average shielding effectiveness of 38.5 dB and a maximum value of 47.8 dB at 12 GHz. In addition, the HV-CMM shows rapid and uniform electrothermal response, reaching a temperature of 143 °C within 150 s under an applied voltage of 1 V. The introduction of a Ni passivation layer significantly enhances environmental stability, reducing the variation in sheet resistance from 152.9% for pure Cu to 42.4% after 240 h under 85 °C/85% RH conditions. This work presents a structure–material co-design strategy, providing a new pathway for multifunctional transparent conductive meshes in applications such as optical windows, defogging/deicing systems, and electromagnetic protection.

Received 26th March 2026
Accepted 22nd April 2026

DOI: 10.1039/d6ra02506d

rsc.li/rsc-advances

1. Introduction

The rapid proliferation of wireless communications, portable electronics, and Internet-of-Things systems has led to increasingly complex electromagnetic environments.[1–3] Consequently, electromagnetic-shielding optical windows have become essential components in advanced optoelectronic systems.[4–6] Conventional EMI shielding materials, such as bulk metals and continuous conductive films,[7–10] rely on high electrical conductivity to reflect and absorb electromagnetic waves; however, they inherently suffer from poor visible-light transmittance, limiting their applicability in transparent devices.

To overcome this limitation, metal mesh-based transparent shielding structures have been extensively explored,[11,12] where optical transmittance and shielding effectiveness can be tuned by adjusting linewidth, periodicity, and fill factor. However, most reported designs employ strictly periodic geometries,[13–17] whose inherent spatial periodicity induces pronounced optical diffraction in the visible range, resulting in discrete diffraction orders and degraded imaging quality.[18–22]

To mitigate such directional diffraction, aperiodic or random architectures,[23–25] including crackle-template-derived meshes,[26–30] have been proposed. While these structures effectively suppress diffraction, their stochastic nature makes it difficult to achieve systematic optimization and reproducible fabrication. In addition, random formation processes limit structural uniformity and scalability over large areas. Therefore, developing a structure that simultaneously enables diffraction suppression and controllable, scalable fabrication remains a key challenge.

To address this issue, we propose a hexagonal–Voronoi composite metal mesh (HV-CMM) as a multifunctional platform that integrates periodic and stochastic features. A continuous hexagonal framework serves as a conductive backbone, ensuring low sheet resistance (R_s) and stable electrical pathways. Meanwhile, embedded Voronoi-type substructures disrupt long-range periodicity at the microscale, thereby suppressing directional diffraction and improving optical uniformity. Furthermore, a Cu/Ni composite system is employed, where Cu provides high electrical conductivity and Ni enhances environmental stability and interfacial durability.[31]

[a]*State Key Laboratory of Widegap Semiconductor Optoelectronic Materials and Technologies, North University of China, Taiyuan, Shanxi 030051, China*
[b]*The 33rd Research Institute of China Electronics Technology Group Corporation, Taiyuan, Shanxi 030032, China*

The multifunctional performance of the HV-CMM is systematically investigated. The fabricated samples exhibit high and spectrally uniform transmittance (78–83%) in the visible range (380–750 nm), with significantly reduced diffraction compared to conventional periodic meshes. In the 1–18 GHz range, the HV-CMM achieves broadband EMI shielding with effectiveness ranging from 25 to 50 dB. In addition, the structure demonstrates rapid and uniform Joule heating, reaching a steady-state temperature of 143 °C under a 1 V bias. These results highlight a scalable strategy for developing multifunctional transparent systems integrating optical transparency, EMI shielding, and electrothermal functionality.

2. Structure design and fabrication

2.1 Structure design

To simultaneously achieve high visible-light transmittance, low sheet resistance, broadband electromagnetic interference (EMI) shielding, and rapid as well as spatially uniform electrothermal response, a metal mesh topology is proposed by integrating a periodic hexagonal framework with an internal Voronoi-type stochastic substructure (Fig. 1a and b).

The hexagonal backbone provides macroscopic mechanical stability and enables good scalability for large-area fabrication. Within each hexagonal unit, a controllable Voronoi-type random mesh is introduced to disrupt long-range coherence, thereby effectively suppressing optical diffraction. The average characteristic size L of the Voronoi mesh can be continuously tuned by adjusting the density of random seed points per unit area, which is given by:

$$L = \frac{1}{\sqrt{N/A}} \quad (1)$$

where A denotes the total area and N represents the number of random seed points. For effective electromagnetic shielding, the average characteristic size L should be much smaller than the wavelength of the incident microwave radiation. Meanwhile, the transmittance in the visible spectrum is primarily determined by the shading ratio, defined as the ratio of the open area to the total area.

The selection of structural parameters is critical for balancing optical and electromagnetic performance. The hexagonal unit size is designed to achieve a balance between the periodic framework and the embedded random Voronoi substructures. A too-small unit size leads to a highly periodic arrangement with pronounced diffraction effects, while a too-large unit size results in a loss of structural controllability due to excessive randomness. Therefore, an intermediate hexagonal size (500 μm) is adopted to simultaneously ensure diffraction suppression and structural designability.

In addition, the linewidth and characteristic dimensions of the mesh directly influence both optical transmittance and EMI shielding effectiveness. The Voronoi feature size is designed to be much smaller than the wavelength in the 1–18 GHz range, while remaining significantly larger than the wavelength of visible light, thereby enabling effective electromagnetic shielding while maintaining high transparency. Based on these considerations, together with preliminary simulations of linewidth and mesh size effects(Fig. 2a and b) the linewidth is set to 5 μm and the Voronoi feature size is selected to be approximately 62.5 μm.

Regarding the material system, a Cu/Ni composite structure is employed as the conductive medium to balance cost, electrical conductivity, and environmental stability. Copper provides high intrinsic electrical conductivity, ensuring low sheet resistance and efficient Joule heating response, whereas nickel readily forms a Ni-rich passivation layer in ambient conditions, significantly enhancing oxidation resistance, corrosion resistance, and damp-heat reliability.

2.2 Fabrication of metal mesh film

The fabrication process of the composite metal mesh is illustrated in Fig. 3. A high-transmittance K9 glass substrate (1.6 mm thick) is used. To improve interfacial adhesion, a Ti adhesion layer (10 nm) and a Cu seed layer (20 nm) are sequentially deposited *via* DC magnetron sputtering, where the Cu layer serves as the conductive base for electroplating. The predesigned hexagonal–Voronoi pattern is then transferred onto the photoresist *via* UV photolithography. Cu and Ni are subsequently deposited by a two-step electroplating process. Specifically, Cu is electroplated in a copper sulfate electrolyte at 15 mA cm^{-2} for 30–60 s, followed by Ni electroplating at 6 mA cm^{-2} for 1–3 min to form a uniform Ni overlayer. Afterward, the photoresist is removed using acetone, and residual metal films in unpatterned regions are eliminated by ion beam etching. This process yields a large-area hexagonal–Voronoi composite metal mesh with uniform linewidth and high structural fidelity.

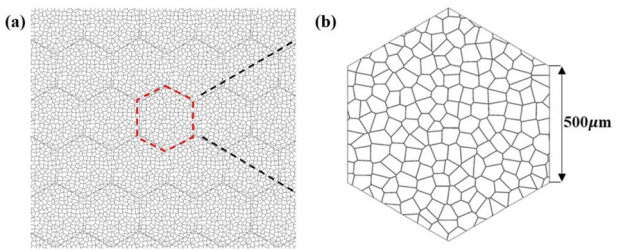

Fig. 1 (a) Schematic illustration of the proposed HV-CMM. (b) Geometric details of a single unit cell.

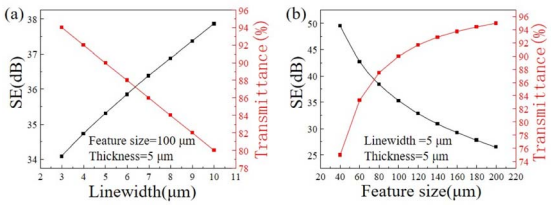

Fig. 2 Effect of structural parameters on the optical transmittance and EMI shielding effectiveness of Cu mesh structures. (a) Linewidth. (b) Mesh feature size.

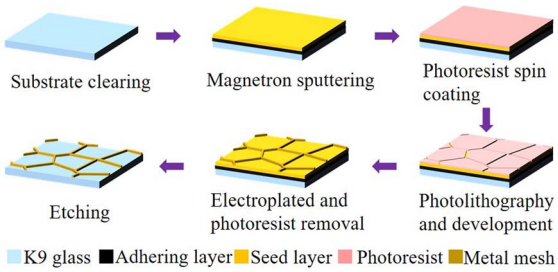

Fig. 3 Schematic illustration of the fabrication process of the mesh.

Based on the above fabrication process, transparent conductive metal meshes were successfully prepared. To ensure the reproducibility of the fabrication process, multiple samples were independently fabricated under identical conditions, and consistent structural and performance characteristics were obtained. By tuning the electroplating time and current density, three groups of samples with different metal thickness configurations were obtained, denoted as Cu_5, Cu_4/Ni_1, and Cu_3/Ni_2, where the subscripts represent the thicknesses (in μm) of the Cu and Ni layers, respectively, with a fixed total metal thickness of 5 μm.

Optical microscopy and scanning electron microscopy (SEM) images reveal uniform linewidths and high pattern fidelity of the metal meshes (Fig. 4a–c). The linewidth is approximately 5 μm, with an average Voronoi cell size of ~62.5 μm and a hexagonal side length of 500 μm. Profilometry measurements further confirm a uniform overall metal thickness of 5 μm across the samples (Fig. 4d).

To analyze the compositional characteristics of the metal mesh structures, X-ray diffraction (XRD) measurements were performed on both pure Cu samples and Cu/Ni composite samples (Fig. 5). The results show that, within the 40°–55° range, the pure Cu sample exhibits two prominent diffraction peaks located at 43.3° and 50.4°, corresponding to the (111) and (200) planes of face-centered cubic Cu, respectively. In contrast, the Cu/Ni composite samples display four diffraction peaks in the same range, located at 43.3°, 44.5°, 50.4°, and 51.9°, which can be attributed to the (111) and (200) planes of fcc Cu and Ni, respectively.

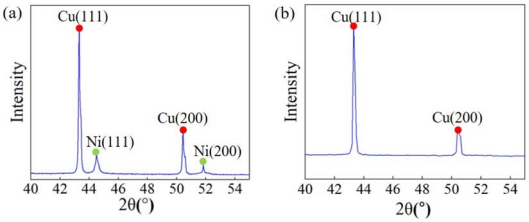

Fig. 5 (a) XRD patterns of the Cu/Ni mesh. (b) XRD patterns of the Cu mesh.

3. Results and discussion

3.1 Optical transmittance and diffraction behavior

Optical transmittance is a key performance metric for transparent conductive materials. The transmittance of the metal mesh samples was characterized over the visible wavelength range of 380–750 nm using a UV-vis spectrophotometer (Fig. 6a).

All samples exhibit high and spectrally uniform transmittance across the visible region, with average values ranging from 78% to 83%. Only minor differences in transmittance are observed among samples with different Cu/Ni thickness ratios, indicating that, under fixed geometric parameters such as linewidth, unit size, and metal coverage ratio, the optical transmittance is primarily governed by the metal coverage rather than the specific material composition. In addition, haze measurements show that the haze values remain within 4.5–4.8% at a wavelength of 600 nm, demonstrating excellent visual transparency (Fig. 6b).

In addition to optical transmittance, visual uniformity and diffraction behavior are critical issues for transparent metal meshes in optical window applications. Since the characteristic feature size of the mesh is much larger than the wavelength of visible light, its optical response is primarily governed by the spatial frequency spectrum of the aperture structure. According to Fourier optics theory, under Fraunhofer conditions, the far-field diffraction intensity can be expressed as the squared magnitude of the two-dimensional Fourier transform of the aperture function $A(x, y)$.

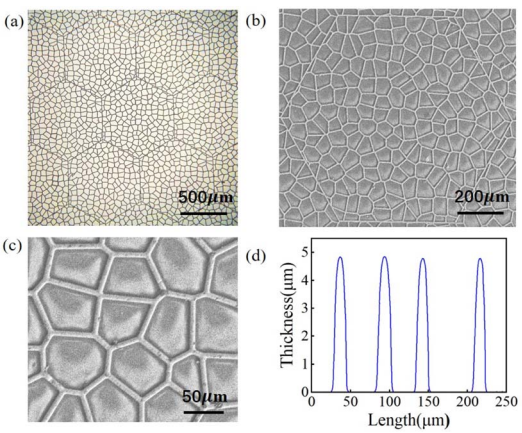

Fig. 4 (a–c) OM and SEM images of the mesh. (d) Thickness distribution of the mesh.

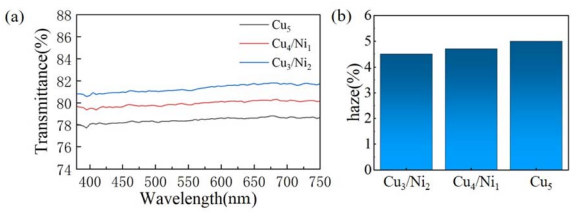

Fig. 6 (a) Optical transmittance spectra of the mesh. (b) Haze values of the mesh.

$$I(k_x,k_y) = |F\{A(x,y)\}|^2 \quad (2)$$

For a periodic hexagonal mesh, the spatial frequency spectrum corresponds to a discrete reciprocal lattice, with optical energy concentrated in a limited number of Bragg diffraction orders, resulting in pronounced directional diffraction and fringe patterns. In contrast, the hexagonal–Voronoi composite mesh introduces stochastic substructures that disrupt long-range periodicity, transforming the frequency spectrum into a convolution of discrete and continuous components. This redistributes the optical energy over a broader frequency range, thereby suppressing and broadening the Bragg peaks.

Two-dimensional fast Fourier transform (FFT) simulations were conducted to analyze both structures (Fig. 7a and b). The periodic mesh exhibits distinct discrete diffraction peaks, with energy concentrated in the zeroth and higher-order modes, whereas the composite mesh shows a quasi-continuous distribution centered at zero frequency with smooth decay, indicating effective suppression of coherent diffraction. Further far-field diffraction experiments are consistent with the simulations (Fig. 7c): the periodic mesh displays well-defined, high-contrast diffraction fringes, while the composite mesh exhibits diffused patterns with reduced fringe contrast and a more uniform background, with no pronounced directional diffraction features observed. These results confirm the effective suppression of long-range coherent scattering by the composite structure.

3.2 Electromagnetic shielding performance

The electromagnetic shielding effectiveness is generally composed of reflection loss, absorption loss, and multiple reflection loss. For metal mesh structures, reflection is typically the dominant shielding mechanism due to the significant impedance mismatch between free space and the highly conductive network. The reflection process is closely related to the electrical conductivity of the material and mainly occurs at the material surface. Absorption is another important shielding mechanism, and its contribution gradually increases with increasing frequency. It is responsible for the dissipation and attenuation of electromagnetic waves after they penetrate into the shielding material. The absorption process can be attributed to dielectric loss (including polarization loss and ohmic loss) as well as magnetic loss.[1,32]

In this work, the continuous Cu network with low sheet resistance provides efficient conductive pathways. When electromagnetic waves impinge on the mesh surface, the pronounced impedance mismatch at the air–metal interface leads to substantial reflection of the incident waves. In addition to reflection, absorption loss also contributes to electromagnetic attenuation through ohmic dissipation. The interconnected conductive network supports induced currents under electromagnetic excitation, and part of the electromagnetic energy is converted into heat *via* Joule heating. Furthermore, due to its relatively high magnetic permeability, Ni can enhance electromagnetic attenuation through magnetic loss.[33]

The electromagnetic shielding effectiveness (SE) of the samples was measured using a vector network analyzer (Fig. 8a). The HV-CMM maintains stable shielding performance over the 1–18 GHz frequency range, with an average shielding effectiveness of 38.5 dB and a maximum value of 47.8 dB at 12 GHz, without noticeable degradation across the measured band. For samples with different metal layer configurations, the shielding effectiveness increases with increasing Cu thickness. Notably, even with higher Ni content, the average shielding effectiveness remains above 35 dB, indicating that the Ni overlayer has only a limited impact on shielding performance.

It is worth noting that, unlike continuous conductive films, the shielding effectiveness of the mesh structure exhibits a non-monotonic dependence on frequency, which has also been reported in previous studies on metallic mesh systems.[34,35] In the present work, a decrease–increase–decrease trend is observed. This behavior can be understood as a result of the frequency-dependent interplay among reflection, absorption, and transmission processes in the conductive mesh structure. As the frequency varies, the relative contributions of these mechanisms evolve, leading to the observed non-monotonic shielding response.

To further elucidate the relationship between shielding effectiveness and electrical properties, the average EMI SE over 1–18 GHz is compared with the corresponding sheet resistance for the three samples (Fig. 8b). The results show that the average shielding effectiveness decreases with increasing sheet resistance, indicating a general negative correlation between electrical conductivity and EMI shielding performance. It should be noted that shielding effectiveness arises from the combined

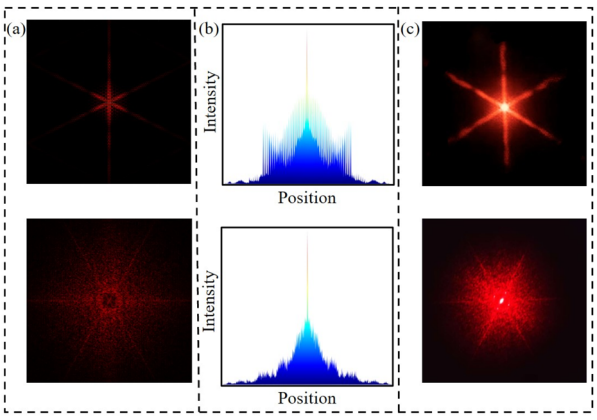

Fig. 7 (a) Simulated far-field diffraction patterns. (b) Normalized diffraction energy distributions (log scale). (c) Experimental far-field diffraction patterns.

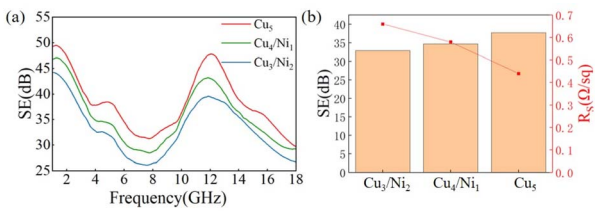

Fig. 8 (a) Electromagnetic shielding effectiveness of HV-CMM samples. (b) SE *vs.* sheet resistance of HV-CMM samples.

contributions of reflection and absorption mechanisms. In the present system, while the Ni layer may introduce additional attenuation, its effect is limited due to its small thickness. Therefore, the observed trend is primarily governed by the sheet resistance of the conductive network, rather than a simple inverse proportional relationship.

3.3 Electrothermal performance

To ensure reliable operation of transparent EMI shielding windows under practical conditions, effective electrothermal performance is essential for mitigating degradation caused by icing, fogging, and condensation. Therefore, the electrothermal behavior of the hexagonal–Voronoi composite metal mesh (HV-CMM) was systematically evaluated.

Under an applied voltage of 1 V, all samples exhibit rapid Joule heating, reaching thermal equilibrium within 100–150 s, with steady-state temperatures ranging from 128 to 143 °C (Fig. 9a). Among them, the Cu_5 sample shows the highest temperature (~143 °C), followed by Cu_4/Ni_1 (~134 °C) and Cu_3/Ni_2 (~128 °C). This trend indicates that increasing Cu thickness enhances electrothermal performance due to reduced sheet resistance and increased Joule heating power density.

The Cu_4/Ni_1 sample was further evaluated under voltages from 0.25 to 1.0 V (Fig. 9b and c). The current rapidly stabilizes and shows an approximately linear dependence on voltage. Both heating rate and steady-state temperature increase monotonically with voltage, reaching ~37, 56, 90, and 134 °C at 0.25, 0.5, 0.75, and 1.0 V, respectively. This behavior follows the Joule heating relationship ($P \propto V^2/R$). Infrared imaging reveals a highly uniform temperature distribution without noticeable hot spots (Fig. 9d), demonstrating the strong potential of the HV-CMM for transparent heating, defogging, and adaptive thermal management.

3.4 Environmental stability

To evaluate the electrical stability of the HV-CMM under harsh environmental conditions, the fabricated samples were subjected to accelerated aging in a temperature–humidity chamber. The test conditions were set at 85 °C and 85% relative humidity (RH). The sheet resistance of the samples was measured every 24 h using a four-point probe method (Fig. 10).

After 240 h, the sheet resistance of the pure Cu mesh increased from 0.49 Ω per sq to 1.27 Ω per sq, corresponding to a variation of approximately 152.9%, indicating significant performance degradation. In contrast, the Cu/Ni composite meshes exhibit markedly reduced variation: the Cu_4/Ni_1 sample increases from 0.58 Ω per sq to 1.05 Ω per sq (81%), while the Cu_3/Ni_2 sample increases from 0.66 Ω per sq to 0.94 Ω per sq (42.4%).

These results demonstrate that the introduction of a Ni passivation layer effectively suppresses resistance drift under damp-heat conditions. This improvement can be attributed to

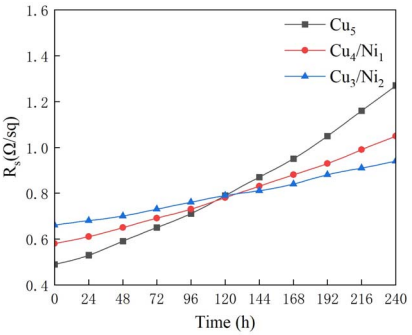

Fig. 10 Sheet resistance of HV-CMM samples under damp-heat aging.

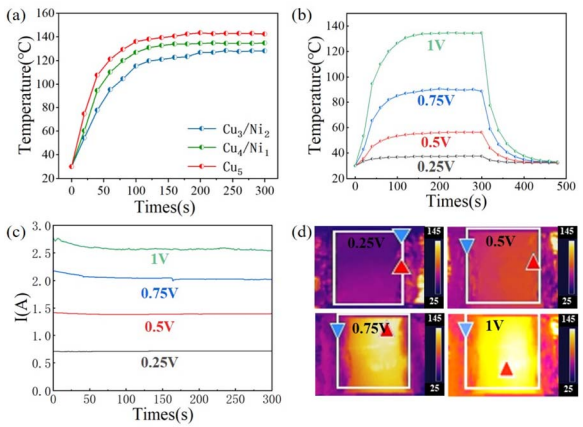

Fig. 9 (a) Surface temperature evolution at 1 V for different Cu/Ni thickness ratios. (b) Temperature–time curves and (c) corresponding current–voltage characteristics of the Cu_4/Ni_1 sample. (d) Infrared thermal images of the Cu_4/Ni_1 sample under different voltages.

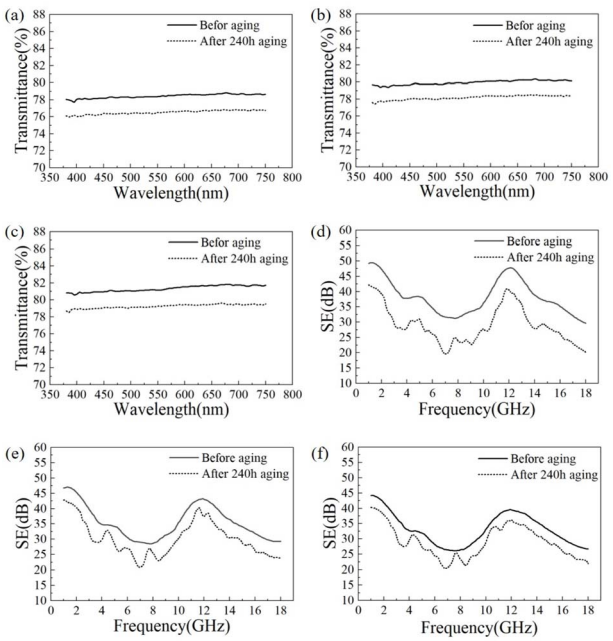

Fig. 11 Transmittance and SE of the samples before and after damp-heat aging. (a–c) Transmittance of Cu_3Ni_2, Cu_4Ni_1, and Cu_5 before and after aging, respectively. (d–f) SE of Cu_3Ni_2, Cu_4Ni_1, and Cu_5 before and after aging.

Table 1 Comparison of the performance of representative transparent EMI shielding materials

Material	Transmittance(%)	SE (dB)	R_s (Ω per sq)	Electrothermal	Oxidation stability	Ref.
ITO/PI	>80	~16	~150	—	—	36
graphene/Al network	~93	~18	~20	—	Intrinsic chemical stability of graphene	37
AgNWs	97	25	~23	50 °C(6V)	Oxidation-prone	38
MXene/AgNWs/MXene	85.1	27.1	8.3	85.6 °C(5V)	R_s ↑ ~30%, MXene isolates from air	39
Cu mesh/PDMS	~85.8	40.4	~0.33	110 °C(1V)	PDMS isolates from air	31
This work	**83**	**38.5**	**~0.58**	**134°C (1V)**	**R_s↑ ~42.4%, Ni protection**	—

the formation of a dense Ni-rich oxide layer, which inhibits moisture penetration and mitigates the oxidation of the underlying Cu, thereby preserving electrical conductivity.

To further evaluate the oxidation stability, the electromagnetic shielding effectiveness and optical transmittance of the samples were measured after 240 h of damp-heat aging. The results show that the optical transmittance remains nearly unchanged before and after aging, with variations within 4% for all samples (Fig. 11a–c). This is because the metal coverage ratio is primarily determined by the physical dimensions of the mesh, which are not significantly altered by surface oxidation. Consequently, the overall transmittance remains stable. In contrast, the EMI shielding effectiveness exhibits a noticeable decrease after aging. Specifically, the SE values of Cu_5, Cu_4Ni_1, and Cu_3Ni_2 decrease by 9.2 dB, 5.3 dB, and 4.1 dB, respectively(Fig. 11d–f). This degradation is attributed to the fact that oxidation primarily affects the continuity of the conductive network, increasing the sheet resistance and reducing the ability to reflect and attenuate electromagnetic waves. These results indicate that the introduction of the Ni protective layer effectively mitigates oxidation-induced performance degradation (Table 1).

4. Conclusions

In summary, a hexagonal–Voronoi composite metal mesh (HV-CMM) has been developed through a synergistic design of hierarchical structure and Cu/Ni material system to achieve multifunctional performance. The introduction of Voronoi stochastic substructures effectively suppresses coherent diffraction by redistributing optical energy in the spatial frequency domain, thereby improving visual uniformity without sacrificing transparency.

The HV-CMM exhibits high optical transmittance (78–83%) and low haze, together with stable EMI shielding performance over a wide frequency range (1–18 GHz), achieving an average shielding effectiveness of 35.5 dB. The results reveal a clear inverse relationship between shielding effectiveness and sheet resistance, emphasizing the critical role of electrical conductivity. Furthermore, the mesh demonstrates rapid and uniform electrothermal behavior, with voltage-dependent heating characteristics governed by Joule heating. The incorporation of a Ni overlayer significantly enhances environmental durability by suppressing moisture-induced oxidation and stabilizing conductive pathways, leading to markedly improved damp-heat stability.

Overall, this study establishes an effective approach for designing transparent conductive meshes that simultaneously meet the demands of optical transparency, EMI shielding, electrothermal functionality, and environmental reliability, offering strong potential for applications in smart windows, defogging systems, and adaptive electromagnetic protection.

Author contributions

Xiaolin Li: conceptualization, data curation, formal analysis, visualization, writing original draft, investigation and methodology; Dianyu Wu: investigation; Xiaoli Xu: methodology; Wenping Geng*: funding acquisition, supervision and writing – review & editing.

Conflicts of interest

There are no conflicts of interest to declare.

Data availability

The data supporting this study are available from the corresponding authors upon reasonable request.

Acknowledgements

This work was supported by the Shanxi Provincial Key Research and Development Program (202402030201007).

References

1 A. A. Isari, A. Ghaffarkhah, S. A. Hashemi, S. Wuttke and M. Arjmand, *Adv. Mater.*, 2024, **36**, 2310683.
2 J. Cheng, C. Li, Y. Xiong, H. Zhang, H. Raza, S. Ullah, J. Wu, G. Zheng, Q. Cao, D. Zhang, Q. Zheng and R. Che, *Nano-Micro Lett.*, 2022, **14**, 80.
3 Z. Yang, Q. Hao, S. Zhang, X. Sun, W. Tian and F. Liu, *Opt. Express*, 2023, **31**, 26355.
4 Y. Cheng, W. Zhu, X. Lu and C. Wang, *Nano Res.*, 2022, **15**, 9595–9613.
5 C. Zhang, C. Ji, Y. Park and L. J. Guo, *Adv. Opt. Mater.*, 2021, **9**, 2001298.
6 C. Yuan, J. Huang, Y. Dong, Y. Lu, J. Li, W. Liu, G. Tang, S. Zhong and W. Song, *Opt. Lett.*, 2021, **46**, 1648.

7 Z. Liu, Y. Zou, C. Ji, X. Chen, G. Hou, C. Zhang, X. Wan, L. J. Guo, Y. Zhao and X. Zhang, *ACS Appl. Mater. Interfaces*, 2021, **13**, 58539–58551.
8 C. Ruan, Q. Sun, D. Xiao, H. Li, G. Xia and S. Wang, *Ceram. Int.*, 2022, **48**, 12317–12323.
9 Y. Zhang, Z. Liu, C. Ji, X. Chen, G. Hou, Y. Li, X. Zhou, X. Cui, X. Yang, C. Ren, D. Liu, L. J. Guo, Y. Zhao and X. Zhang, *ACS Appl. Energy Mater.*, 2021, **4**, 6553–6561.
10 R. Xu, X. Zhang, D. Zhang, J. Liu, J. Lu, R. Zhao, Y. Ji, F. Qian, H. Wang, J. Fan, W. Li and H. Yang, *J. Alloys Compd.*, 2022, **890**, 161897.
11 Z. Jiang, S. Zhao, W. Huang, L. Chen and Y. Liu, *Opt. Express*, 2020, **28**, 26531.
12 S. H. Ryu, Y. K. Han, S. J. Kwon, T. Kim, B. M. Jung, S. B. Lee and B. Park, *Chem. Eng. J.*, 2022, **428**, 131167.
13 Z. Qiu, Z. Sun, M. Hu, L. Zhao and S. Yu, *Opt. Mater.*, 2024, **155**, 115926.
14 M. Li, M. Zarei, K. Mohammadi, S. B. Walker, M. LeMieux and P. W. Leu, *ACS Appl. Mater. Interfaces*, 2023, **15**, 30591–30599.
15 S. Chung, P. K. Kim and T. Ha, *J. Manuf. Syst.*, 2023, **33**, 035002.
16 Y. Liang, X. Huang, J. Pan, W. Liu, K. Wen, D. Zhai, P. Shang and P. Liu, *Adv. Mater. Technol.*, 2023, **8**, 2201532.
17 Z. Liang, Z. Zhao, M. Pu, J. Luo, X. Xie, Y. Wang, Y. Guo, X. Ma and X. Luo, *Opt. Mater. Express*, 2020, **10**, 796.
18 H. Wang, Z. Lu, Y. Liu, J. Tan, L. Ma and S. Lin, *Opt. Lett.*, 2017, **42**, 1620.
19 H. Wang, Z. Lu and J. Tan, *Opt. Express*, 2016, **24**, 22989.
20 W. Wang, B. Bai, Q. Zhou, K. Ni and H. Lin, *Opt. Mater. Express*, 2018, **8**, 3485.
21 Z. Jiang, W. Huang, L. Chen and Y. Liu, *Opt. Express*, 2019, **27**, 24194.
22 Y. Wu, Q. Li and Y. Li, *Carbon*, 2024, **229**, 119474.
23 D. Liao, Y. Zheng, X. Ma and Y. Fu, *Opt. Express*, 2023, **31**, 32200.
24 Y. Liu, C. Yang, Y. Wang, Y. Shao, T. Zheng, K. Yuan, Y. Cheng, Y. Zhang and W. Shen, *Opt. Express*, 2024, **32**, 30156.
25 H. Zhong, Y. Han and J. Lin, *Opt. Express*, 2020, **28**, 7008.
26 Y. Han, J. Lin, Y. Liu, H. Fu, Y. Ma, P. Jin and J. Tan, *Sci. Rep.*, 2016, **6**, 25601.
27 A. S. Voronin, Y. V. Fadeev, I. V. Govorun, I. V. Podshivalov, M. M. Simunin, I. A. Tambasov, D. V. Karpova, T. E. Smolyarova, A. V. Lukyanenko, A. A. Karacharov, I. V. Nemtsev and S. V. Khartov, *J. Mater. Sci.*, 2021, **56**, 14741–14762.
28 L. Yang, Y. Guan, F. Gao, R. Wan and P. Wang, *Results Eng.*, 2025, **25**, 103888.
29 Y. Yu. Tarasevich, A. V. Eserkepov and I. V. Vodolazskaya, *Phys. Rev. E*, 2023, **108**, 044143.
30 Y. Han, Y. Liu, L. Han, J. Lin and P. Jin, *Carbon*, 2017, **115**, 34–42.
31 Z. Chen, S. Yang, J. Huang, Y. Gu, W. Huang, S. Liu, Z. Lin, Z. Zeng, Y. Hu, Z. Chen, B. Yang and X. Gui, *Nano-Micro Lett.*, 2024, **16**, 92.
32 H. Yao, J. Yang, H. Li, J. Xu and K. Bi, *Adv. Compos. Hybrid Mater.*, 2023, **6**, 43.
33 Z. Fu, Y. Wu, Y. Li, K. Huang, Q. Li, H. Yao, W. Cao, S. Gao, K. Bi, H. Wu, *et al.*, *J. Materiomics*, 2025, **11**, 100936.
34 Y. Liang, X. Huang, K. Wen, Z. Wu, L. Yao, J. Pan, W. Liu and P. Liu, *Appl. Sci.*, 2023, **13**, 4846.
35 S. A. Voronin, B. A. Parshin, M. O. Makeev, P. A. Mikhalev, Y. V. Fadeev, F. S. Ivanchenko, I. I. Bril, I. A. Tambasov, M. M. Simunin and S. V. Khartov, *Materials*, 2025, **18**, 4102.
36 Y. Kim, S.-K. Hyeong, Y. Choi, S.-K. Lee, J.-H. Lee and H. K. Yu, *ACS Appl. Mater. Interfaces*, 2021, **13**, 61413–61421.
37 L. Ma, Z. Lu, J. Tan, J. Liu, X. Ding, N. Black, T. Li, J. Gallop and L. Hao, *ACS Appl. Mater. Interfaces*, 2017, **9**, 34221–34229.
38 X. Liang, J. Lu, T. Zhao, X. Yu, Q. Jiang, Y. Hu, P. Zhu, R. Sun and C. Wong, *Adv. Mater. Interfaces*, 2019, **6**, 1801635.
39 Y.-S. Zhang, T. Wang, Z.-L. Bao, P.-F. Qian, X.-C. Liu, W.-H. Geng, D. Zhang, S.-W. Wang, Q. Zhu and H.-Z. Geng, *J. Colloid Interface Sci.*, 2024, **665**, 376–388.